Storage-Based Frequency Shaping Control

Yan Jiang, Eliza Cohn, Petr Vorobev, *Member, IEEE*, and Enrique Mallada, *Senior Member, IEEE*

***Abstract*—With the decrease in system inertia, frequency security becomes an issue for power systems around the world. Energy storage systems (ESS), due to their excellent ramping capabilities, are considered as a natural choice for the improvement of the frequency response following major contingencies. In this paper, we propose a new strategy for energy storage – *frequency shaping control* – that allows to completely eliminate the frequency Nadir, one of the main issues in frequency security, and at the same time tune the rate of change of frequency (RoCoF) to a desired value. With Nadir eliminated, the frequency security assessment can be performed via simple algebraic calculations, as opposed to dynamic simulations for conventional control strategies. Moreover, our proposed control is also very efficient in terms of the requirements on storage peak power, requiring less (up to 40% in one of the cases) power than conventional virtual inertia approach for the same performance.**

***Index Terms*—Electric storage, frequency control, frequency Nadir, rate of change of frequency, low-inertia power systems.**

I. Introduction

The reduction of system inertia, caused by the replacement of conventional synchronous generation with renewable energy sources, is one of the biggest challenges for frequency control in power systems [1]. Lower inertia causes larger frequency deviations during transients, even if the system has adequate primary reserves to keep the steady-state frequency deviation within acceptable limits [2]. The so-called frequency Nadir – the lowest value of the frequency during transients – can become unacceptable for low-inertia systems, which in turn is sometimes regarded as the main reason for limiting further increase of renewable generation penetration [3], [4]. Fortunately, the recent advancements in power electronics and electric storage technologies provide the potential to mitigate this issue through the use of inverter-interfaced storage units that can provide additional frequency response. With proper controllers, fast inverter dynamics can ensure the rapid response from storage devices.

A straightforward control approach for energy storage systems (ESS) is to let energy storage units provide simple proportional power-frequency response similar to conventional synchronous generators [5]. However, unlike synchronous generators that produce a delayed response to the control signal, the response of storage units is almost instantaneous. This can help arrest the frequency drop during the first few seconds following a disturbance, while generator turbines are gradually increasing their power output. Moreover, because of the absence of delays, smaller droop coefficients (larger gains) are accessible for energy storage units, which makes them even more efficient during sudden frequency disturbances [6]. For example, an impressive $472\,\mathrm{MW}$ of storage has been reported to participate in the frequency response during the recent blackout in the Great Britain system on August 9, 2019 [7]. A drawback of this droop control strategy is that the storage units will continue to provide their response as long as the system frequency is away from its nominal value, which can lead to rather high requirements on storage capacity.

Another common control approach is the so-called "synthetic inertia" (also referred to as "virtual inertia" (VI)), where energy storage units imitate the natural inertial response of synchronous machines, thus compensating for the lack of physical inertia [8], [9]. Such a control strategy is especially efficient in reducing the frequency Nadir as well as the initial RoCoF, following sudden power imbalances. The topic is widely discussed in literature. We will provide a brief survey of the most relevant sources, yet a comprehensive review is given in [10]. There are various approaches for VI implementation: by wind turbines [11], by electric vehicles [12], by distributed energy resources [13], and by controlling DC-side capacitors of grid-connected power converters [8]. In a recent paper [14] an important question of VI placement is discussed. Finally, we note that both synthetic inertia (derivative control) and droop (proportional control) can be combined into a single control strategy. Sometimes, it is this combined strategy that is referred to as VI.

It is evident that, in many of the power systems around the world, storage facilities can become the main tool for executing frequency control, especially following contingencies, where speed or response is of vital importance. While both synthetic inertia and droop response can be rather effective in improving the frequency transient performance, energy storage units have the potential of implementing a much wider class of control strategies. A high level goal for such strategies would be to provide certain frequency response while minimizing the cost of storage units. The later is mostly determined by the energy and power capacity of storage units required to execute certain strategy. In the present paper, we develop a novel control strategy – *frequency shaping control* – that guarantees frequency transients without Nadir, while at the same time keeping RoCoF and steady-state frequency deviation within pre-specified limits. We emphasize that eliminating the frequency Nadir means much more than just improving the transient frequency response: it allows to completely change the frequency security assessment procedure by reducing it to simple algebraic operations, rather than dynamic simulations.

Y. Jiang, E. Cohn, and E. Mallada are with the Electrical and Computer Engineering Department, Johns Hopkins University, Baltimore, MD 21218, USA. E-mails: yjiang@jhu.edu, eliza.cohn1@gmail.com, mallada@jhu.edu.

P. Vorobev is with the Energy Department, Skolkovo Institute of Science and Technology, Moscow 143026, Russia. E-mail: p.vorobev@skoltech.ru.

This work was supported by NSF through grants CAREER 1752362, EPCN 1711188, AMPS 1736448, and TRIPODS 1934979, Johns Hopkins University Discovery Award and Catalyst Award.

The main contributions of the paper are as follows:

1) We analyze the performance of traditional VI control and show its drawbacks, especially in terms of excessive control effort required from the storage.
2) We propose a new control strategy for storage – *frequency shaping control* – that allows to turn the system frequency dynamics into a first-order one, thus eliminating frequency Nadir. We show that this strategy requires less storage power capacity compared to conventional VI.
3) We generalize our control strategy for multi-machine systems with arbitrary governor and turbine models and show how it can be tuned to satisfy constraints on RoCoF and steady-state frequency deviation.

The rest of this paper is organized as follows. Section II describes the single-area power system model and defines performance metrics. Section III analyzes the performance and limitations of VI control so as to motivate the need for a new control strategy. Section IV describes the proposed frequency shaping control, shows how it outperforms VI, and generalizes it for multi-machine systems. Section V validates our results through detailed simulations. Section VI concludes the paper.

II. Modelling Approach and Problem Statement

A. System Model

We start by considering dynamics of a center of inertia (COI) of a single-area power system so that the whole system can be modelled as an equivalent synchronous machine. Such a representation is proven to be sufficiently accurate for many practical systems [15]–[17]. The generalization to multi-machine representation will be described in Section IV-C. Frequency dynamics of such a system can be described by the conventional swing equation:

$$\frac{2H}{\Omega_0}\dot{\Omega} = P_\mathrm{m} - P_\mathrm{L} + P_\mathrm{b}\,, \tag{1}$$

where H is the combined inertia constant of the system (in second), Ω is the system frequency (in radian per second), $\Omega_0 := 2\pi F_0$ is the nominal frequency ($F_0 = 50\,\mathrm{Hz}$), P_m is the total mechanical power supplied to the system (in per unit), P_L is the total load demand (in per unit), and P_b is the total power supplied by the storage system (in per unit), which also includes any frequency control actions. In this paper, we will be mostly interested in dynamics of the system (1) subject to a sudden power imbalance ΔP.

In order to study the frequency dynamics, it is convenient to consider the deviations of all the variables from their equilibrium values. Thus, we will denote as ω the per unit deviation of frequency from its nominal value, i.e.,

$$\omega = \frac{\Omega - \Omega_0}{\Omega_0}\,. \tag{2}$$

For convenience, we will also use $f := F_0\omega$ in the paper. Likewise, p_m, p_L, and p_b will be used to denote the per unit variations of mechanical power input, electric power demand, and storage power output from their respective nominal values.

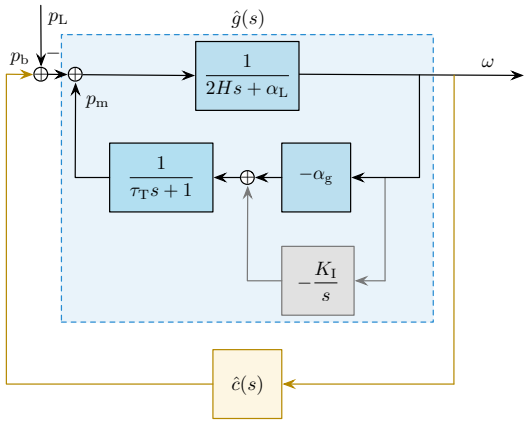

Fig. 1. Block diagram of an aggregated power system with frequency control from generators and storage units.

With such denotations, the frequency dynamics of the system under study can be described by the following equations:

$$\dot{\theta} = \Omega_0\omega\,, \tag{3a}$$

$$2H\dot{\omega} = p_\mathrm{m} - p_\mathrm{L} - \alpha_\mathrm{L}\omega + p_\mathrm{b}\,, \tag{3b}$$

$$\tau_\mathrm{T}\dot{p}_\mathrm{m} = -p_\mathrm{m} - \alpha_\mathrm{g}\omega - K_\mathrm{I}\frac{\theta}{\Omega_0}\,, \tag{3c}$$

$$\dot{E}_\mathrm{b} = p_\mathrm{b}\,, \tag{3d}$$

where E_b is the energy supplied by storage and θ is an auxiliary variable used for the secondary frequency control. The parameters in (3) are defined as follows: τ_T – turbine time constant (in second), α_L – the load-frequency sensitivity coefficient (in per unit), α_g – the aggregate inverse droop of generators (in per unit), and K_I – the aggregate secondary frequency control gain of the system (in per unit per second).

The model described by (3) is shown by a block diagram in Fig. 1. The conventional generator block (with primary and secondary controls) is shaded in blue. We will denote the aggregate transfer function of this block (in Laplace domain) as $\hat{g}(s)$. For clarity of our derivations, we use a simplified first-order turbine representation. The generalization to more complex models will be provided in Section IV-C.

Compared to conventional generators, inverter-interfaced storage have much faster dynamic response rates (few decades of milliseconds) that allow for more control flexibility. Thus, at the timescales of frequency dynamics, we can assume that storage can provide any shape of power response (within the installed capacity capability). We denote the storage frequency response function as $\hat{c}(s)$, i.e.,

$$\hat{p}_\mathrm{b}(s) = \hat{c}(s)\hat{\omega}(s)\,.^{1} \tag{4}$$

The detailed form of $\hat{c}(s)$ depends on a chosen control strategy.

For most of the derivations in the paper, we will use the system parameters corresponding to the Great Britain system [18], [19]. We will use $P_\mathrm{B} = 32\,\mathrm{GVA}$ as a base power, and the value of the maximum power imbalance $\Delta P = 1.8\,\mathrm{GW}$ corresponding to the loss of the two biggest generation units,

[1]We use hat to distinguish the Laplace transform from its time domain counterpart.

as specified in [19]. Under the high renewable penetration scenario, the total inertia of the system is expected to be around $70\,\mathrm{GVA\,s}$ which corresponds to $H = 2.19\,\mathrm{s}$ on the system base. These parameter values are summarized in Table I. For the turbine time constant we use $\tau_\mathrm{T} = 1\,\mathrm{s}$.

TABLE I
PARAMETER VALUES OF POWER SYSTEMS

Parameters	Symbol	Value
System power base	P_B	$32\,\mathrm{GVA}$
Maximum power imbalance	ΔP	$1.8\,\mathrm{GW}$
Inertia time constant	H	$2.19\,\mathrm{s}$
Load sensitivity coefficient	α_L	$1\,\mathrm{pu}$
Aggregate inverse droop of generators	α_g	$15\,\mathrm{pu}$
Secondary frequency control gain	K_I	$0.05\,\mathrm{s}^{-1}$

† All per unit values are on the system power base.

B. Performance Assessment of Frequency Control

Since frequency deviation is volatile in a low-inertia power system, it is necessary to resort to certain measures to ensure frequency security, especially following major disturbances. Notably, for storage-based frequency control strategy design, not only control performance but also economic factors matter [20], [21]. Therefore, the performance metrics that are of our interest for comparing different control strategies are twofold: frequency response metrics and storage economics metrics.

1) Frequency Response Metrics: The factors that are relevant to frequency security are:

- *Steady-state frequency deviation* is the deviation of frequency from the nominal value after all the primary response is activated, i.e.,

$$\Delta\omega := \lim_{t\to\infty} \omega(t) \quad \text{with} \quad K_\mathrm{I} = 0\,. \tag{5}$$

  The maximum allowed quasi-steady-state frequency deviation for the European and Great Britain systems is $\pm 200\,\mathrm{mHz}$ [19], [22].
- *Nadir* is the maximum frequency drop during a transient response, i.e.,

$$|\omega|_\infty := \max_{t\geq 0} |\omega(t)|\,. \tag{6}$$

  For example, the maximum allowed Nadir is $800\,\mathrm{mHz}$ for the European system [20] and $500\,\mathrm{mHz}$ for the Great Britain system [18], [19]. For microgrids, the maximum allowed frequency drop can be specified either by state standards or by some technical rules specific to the microgrid.
- *RoCoF* is the maximum rate of change of frequency, which usually occurs at the initial time instant, i.e.,

$$|\dot\omega|_\infty := \max_{t\geq 0} |\dot\omega(t)|\,. \tag{7}$$

  The highest RoCoF value allowed in the European system is $0.5\,\mathrm{Hz\,s}^{-1}$.

2) Storage Economics Metrics: The two factors that significantly affect the cost of storage units are:

- *Energy capacity* is the maximum amount of energy supply from storage during the whole transient duration, i.e.,

$$E_\mathrm{b,max} := \max_{t\geq 0} E_\mathrm{b}(t)\,. \tag{8}$$

  The maximum amount of energy supply directly determines the required storage capacity which, at present, represents the main contribution to the overall cost of storage systems.
- *Maximum power* is the maximum amount of power output from storage during the whole transient duration, i.e.,

$$p_\mathrm{b,max} := \max_{t\geq 0} p_\mathrm{b}(t)\,. \tag{9}$$

  The maximum power output of the storage unit is also important since lower values of it mean that one can use inverters with lower installed capacity.

III. CONVENTIONAL CONTROL STRATEGY FOR STORAGE

In this section we briefly analyze the most common traditional control strategy for storage-based frequency response – "virtual inertia" (VI). We are mostly interested in its performance from the point of view of improving the Nadir and RoCoF, and we will assess the amount of power and energy required from storage to achieve certain performance level in the system.

The most common VI strategy includes both inertial response (IR) and power-frequency response (PFR). It can be represented by the following effective storage transfer function $\hat c_\mathrm{vi}(s)$:

$$\hat c_\mathrm{vi}(s) := -(m_\mathrm{v} s + \alpha_\mathrm{b})\,,^{2} \tag{10}$$

where m_v is the IR constant and α_b is the PFR constant. We will use the subscript "vi" to refer to this type of control strategy from storage.

For most of the analysis in the paper, when deriving analytic expressions, we will omit the secondary control since its purpose is to gradually drive the frequency back to nominal following a contingency and it does not significantly influence the transient frequency dynamics. Likewise, the load-frequency sensitivity coefficient α_L will also be set to zero when deriving control laws – this coefficient is typically of the order of unity for most power systems and its exact values are usually unknown. Setting α_L to zero will make our results slightly conservative. We note though that all dynamic simulations will be done with secondary control and load-frequency sensitivity coefficient present.

A. Coupled Nadir Elimination and RoCoF Tuning

Under VI control strategy (10), the frequency deviation ω_vi following a step power imbalance in Laplace domain is given by

$$\hat\omega_\mathrm{vi}(s) = \frac{-\Delta P\,(\tau_\mathrm{T} s + 1)}{s\left[\tilde m \tau_\mathrm{T} s^2 + (\tilde m + \tau_\mathrm{T}\alpha_\mathrm{b})\, s + \alpha_\mathrm{tot}\right]}, \tag{11}$$

[2]An additional low-pass filter is needed to make this transfer function proper. In all of our numerical models, we will use a low-pass filter with a cut-off frequency of 5 Hz. For simplicity, we will omit it in formulas.

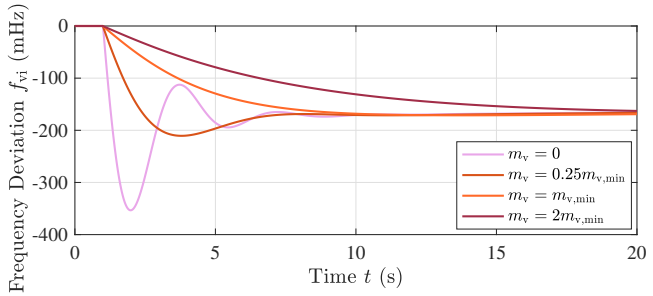

Fig. 2. Frequency deviations under virtual inertia control from storage with $\alpha_{\rm b} = 0$ and different values of $m_{\rm v}$.

where $\tilde{m} := 2H + m_{\rm v}$ is the compensated system inertia and $\alpha_{\rm tot} := \alpha_{\rm g} + \alpha_{\rm b}$ is the aggregate inverse droop of the system.

By the final value theorem, the steady-state frequency deviation is always determined by the aggregate inverse droop of the system as

$$\Delta\omega_{\rm vi} = \lim_{s\to 0} s\hat{\omega}_{\rm vi}(s) = -\frac{\Delta P}{\alpha_{\rm tot}}\,. \tag{12}$$

With our present choice of parameter values from the Great Britain system, the generator droop alone allows to fulfill the requirement on steady-state frequency deviation. This is easily seen by setting $\alpha_{\rm b} = 0$ in (12), which yields $f_{\infty,\rm vi} = -187.5\,\rm mHz$, a value within the range of $\pm 200\,\rm mHz$. In contrast to the irrelevance of the steady-state frequency to the IR constant $m_{\rm v}$, the Nadir and RoCoF significantly depend on the choice of $m_{\rm v}$. As seen in Fig. 2, greater values of $m_{\rm v}$ will lead to decreases of both Nadir and RoCoF.

From the Laplace domain expression (11), the analytic expression for $\omega_{\rm vi}(t)$ can be obtained following standard steps. The resulting expression is, however, rather cumbersome, thus we do not present it here explicitly. In order to find the frequency Nadir $|\omega|_{\infty,\rm vi}$ for arbitrary values of $m_{\rm v}$ and $\alpha_{\rm b}$, one needs to find the value of this function $\omega_{\rm vi}(t)$ at the time instant corresponding to its first minimum. This can be done by following the standard but unwieldy steps, the details of which can be found in [23, Theorem 4]. Fig. 3 provides a plot of $|f|_{\infty,\rm vi}$ as a function of $m_{\rm v}$. It is evident that, for any given value of $\alpha_{\rm b}$, the Nadir gets shallower with the increase of the IR constant $m_{\rm v}$. Moreover, one can entirely remove Nadir by tuning $m_{\rm v}$ to be sufficiently large, where the critical value of $m_{\rm v}$ is determined by the following theorem.[3]

Theorem 1 (Critical value of IR constant for removing Nadir). *For a single-area power system described by* (3) *and* (4)*, the step response under VI control in* (10)*, i.e.,* $\hat{c}(s) = \hat{c}_{\rm vi}(s)$*, has no Nadir if*

$$m_{\rm v} \geq m_{\rm v,min} := \tau_{\rm T}\beta^2 - 2H\,, \tag{13}$$

with $\beta := \sqrt{\alpha_{\rm g}} + \sqrt{\alpha_{\rm tot}}$.

Proof. Nadir occurs only if there exists some non-negative finite time instant $t_{\rm nadir}$ at which $\dot{\omega}_{\rm vi}(t_{\rm nadir}) = 0$. Therefore, a condition on $m_{\rm v}$ ensuring $\dot{\omega}_{\rm vi}(t) = 0$ only when $t = \infty$ suffices to remove Nadir. Applying [23, Theorem 4] to (11), we find that the VI control parameters $(\alpha_{\rm b}, m_{\rm v})$ should satisfy the following relations:

$$\begin{cases} \tilde{m}^2 - 2\tau_{\rm T}\left(\alpha_{\rm b} + 2\alpha_{\rm g}\right)\tilde{m} + \tau_{\rm T}^2\alpha_{\rm b}^2 \geq 0 \\ \tilde{m} - \tau_{\rm T}\alpha_{\rm b} \geq 0 \end{cases}. \tag{14}$$

The first quadratic inequality in $\tilde{m}$ above holds if $\tilde{m} \geq \tau_{\rm T}\left(\sqrt{\alpha_{\rm g}} + \sqrt{\alpha_{\rm tot}}\right)^2$ or $\tilde{m} \leq \tau_{\rm T}\left(\sqrt{\alpha_{\rm g}} - \sqrt{\alpha_{\rm tot}}\right)^2$. However, only the former region satisfies the second condition in (14). This concludes the proof of the desired result. □

If it is recognized that $\alpha_{\rm b}$ is much smaller than $\alpha_{\rm g}$, an approximate expression for $m_{\rm v,min}$ in (13) can be obtained:

$$m_{\rm v,min} = 2\tau_{\rm T}(2\alpha_{\rm g} + \alpha_{\rm b}) - 2H\,. \tag{15}$$

As an illustration, Fig. 4 shows the minimum IR constant requirement $m_{\rm v,min}$ for eliminating the Nadir as a function of the PFR constant $\alpha_{\rm b}$. Both the exact solution from (13) and the linear approximation from (15) are shown to demonstrate the minimal difference between the two. Noticeably, the required $m_{\rm v,min}$ has rather high values, which are usually more than 10 times of the original system inertia $2H = 4.38\,\rm s$.

[3]In this paper, "remove the Nadir" means "remove the frequency response overshoot".

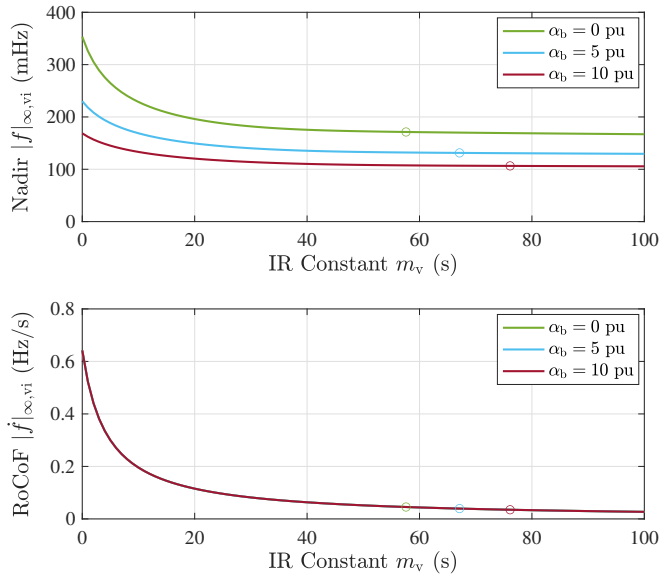

Fig. 3. Effect of the IR constant on Nadir and RoCoF for different chosen values of $\alpha_{\rm b}$, where circles denote the points corresponding to $m_{\rm v} = m_{\rm v,min}$.

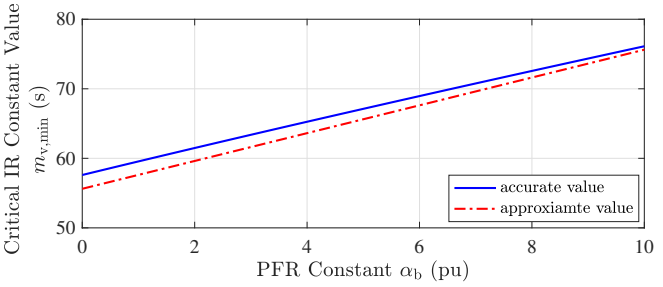

Fig. 4. Minimum IR constant required to eliminate Nadir as $\alpha_{\rm b}$ varies from 0 to 10 pu.

The significance of eliminating the Nadir lies in the fact that the frequency security of the system can be certified by performing only simple *algebraic* calculations so as to avoid running explicit *dynamic* simulations. More precisely, given the expected maximum magnitude of power imbalance ΔP and the acceptable value for steady-state frequency deviation $\Delta\omega_{\mathrm{d}}$, one can simply choose:

$$\alpha_{\mathrm{b}}=\max\left(\left|\frac{\Delta P}{\Delta\omega_{\mathrm{d}}}\right|-\alpha_{\mathrm{g}},0\right) \text{ and } m_{\mathrm{v}}=\max(m_{\mathrm{v,min}},0)\,. \quad (16)$$

Once both m_{v} and α_{b} are determined, one can calculate RoCoF as:

$$|\dot{\omega}|_{\infty,\mathrm{vi}}=\left|\lim_{s\to\infty}s^2\hat{\omega}_{\mathrm{vi}}(s)\right|=\frac{\Delta P}{\tilde{m}}\,, \quad (17)$$

which is inversely proportional to the compensated system inertia. Thus, under the VI control, there is a coupling between Nadir elimination and RoCoF tuning. If one adopts the tuning given in (16), then, excluding the degenerate case $m_{\mathrm{v}}=0$ that rarely occurs, the RoCoF is fixed to be $\Delta P/(2H+m_{\mathrm{v,min}})$. Yet, the high value of $m_{\mathrm{v,min}}$ leads to a too small RoCoF and thus a very long settling time, as shown in Fig. 2. If one hopes to adjust the RoCoF appropriately so as to let the frequency evolves with a moderate rate, then the Nadir cannot be removed. We also note that, according to (15), $m_{\mathrm{v,min}}$ is very sensitive to turbine time constant, and the values shown in Fig. 3 correspond to a rather modest value of $\tau_{\mathrm{T}}=1\,\mathrm{s}$. For slower governors and turbines, the requirements on $m_{\mathrm{v,min}}$ will be even higher.

B. Power and Energy Requirements on Storage

In order to quantify the required amount of power rating of the storage unit for a given control strategy $\hat{c}_{\mathrm{vi}}(s)$, one needs to find the maximum of $p_{\mathrm{b}}(t)$ during the whole transient. The procedure is rather straightforward, but the explicit expression for $p_{\mathrm{b}}(t)$ in time domain is very cumbersome for arbitrary values of m_{v} and α_{b}. The top panel of Fig. 5 shows the maximum storage power as a function of IR constant m_{v} for different values of PFR constant α_{b} (for power/energy requirement figures we use per unit system based on the disturbance size ΔP for simpler comparison). Comparing with the top panel in Fig. 3, we observe that, for m_{v} less than $m_{\mathrm{v,min}}$, the Nadir and power rating are quite sensitive to variations in m_{v}, yet, for m_{v} greater than $m_{\mathrm{v,min}}$, they are practically insusceptible to changes in m_{v}, which implies that $m_{\mathrm{v}}=m_{\mathrm{v,min}}$ plays the role of a saturation point after which an increase in power rating of storage system does not provide any benefit to a decrease in Nadir. This justifies the optimality of Nadir elimination by setting $m_{\mathrm{v}}=m_{\mathrm{v,min}}$.

It is evident from Fig. 5 that, for the special case of $m_{\mathrm{v}}=m_{\mathrm{v,min}}$, the maximum power $p_{\mathrm{b,max}}$ is almost independent of the PFR constant α_{b}, so we can set it to zero to simplify the expression for $p_{\mathrm{b}}(t)$. Thus, for the case $m_{\mathrm{v}}=m_{\mathrm{v,min}}$ and $\alpha_{\mathrm{b}}=0$, one has the following expression:

$$p_{\mathrm{b,vi}}(t)=\Delta P\left(1-\frac{H}{2\tau_{\mathrm{T}}\alpha_{\mathrm{g}}}\right)\left(1+\frac{t}{2\tau_{\mathrm{T}}}\right)e^{-\frac{t}{2\tau_{\mathrm{T}}}}\,, \quad (18)$$

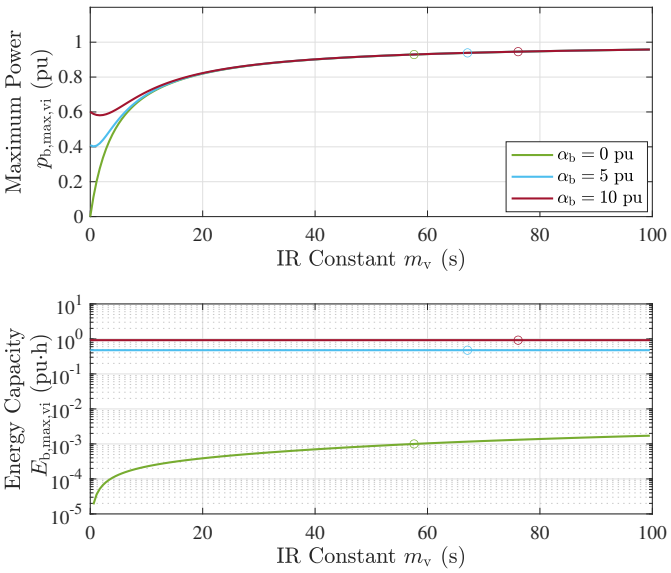

Fig. 5. Effect of the IR constant on maximum power and energy capacity requirements, where circles denote the points corresponding to $m_{\mathrm{v}}=m_{\mathrm{v,min}}$.

for which the maximum value occurs at $t=0$ and is equal to $p_{\mathrm{b,max}}=\Delta P\,[1-H/(2\tau_{\mathrm{T}}\alpha_{\mathrm{g}})]$ and is very close to the disturbance size ΔP for realistic values of parameters.

The storage energy capacity required to execute $\hat{c}_{\mathrm{vi}}(s)$ is predominantly determined by the values of α_{b} and the aggregate secondary control gain K_{I} (the bottom panel in Fig. 5). For zero values of α_{b}, the energy capacity required will be very small (10^{-3} pu·h or less). Note that, in practice, unless α_{b} is substantial, the minimum storage energy capacity will be determined by the C-rate of the batteries used, hence, the exact value of $E_{\mathrm{b,max,vi}}$ is of little importance.[4] For values of α_{b} that are not very small, an approximate formula $E_{\mathrm{b,max,vi}}\approx\alpha_{\mathrm{b}}/K_{\mathrm{I}}$ can be used. This suggests that higher secondary control gains tend to reduce the required storage energy capacity.

To summarize, VI control can be an effective tool to improve transient frequency performance, however, RoCoF and Nadir become coupled under this type of control. Modest amounts of IR from storage can somewhat improve the frequency Nadir. However, complete elimination of Nadir will require massive amounts of IR, which makes it impractical.

IV. Frequency Shaping Control

Although VI control seems to be a straightforward choice, inverter-interfaced storage units are potentially capable of executing a much wider class of control strategies. In this section we propose a novel control strategy – *frequency shaping control* – which is able to decouple the Nadir elimination task from the RoCoF tuning one. The general idea behind the frequency shaping control is to effectively turn the system frequency dynamics into a first-order one, which is dependent on two control parameters, by employing a special form of the

[4] A C-rate measures the rate at which a battery is charged or discharged relative to its rated capacity [24]. For example, a $5\,\mathrm{C}$ rate means that the discharge current will discharge the entire battery in $0.2\,\mathrm{h}$.

storage response function $\hat{c}(s)$. Such a first-order response has no Nadir naturally, while tuning of the two parameters will provide the ability to adjust both the steady-state frequency deviation and the RoCoF, independently.

A. Controller Design

For designing the needed frequency shaping control (which we will denote as $\hat{c}_{\rm fs}(s)$), let us consider a second-order transfer function of the following form:[5]

$$\hat{c}_{\rm fs}(s) := -\frac{A_1 s^2 + A_2 s + A_3}{\tau_{\rm T} s + 1}\,, \tag{19}$$

where $\tau_{\rm T}$ is the system turbine time constant from (3c), A_1, A_2, and A_3 are tunable control parameters. Then, the desired frequency shaping control is determined by the next theorem.

Theorem 2 (Frequency shaping). *The single-area system in Fig. 1 will respond to a power imbalance $-p_{\rm L}$ as a first-order system of the form:*

$$\hat{h}(s) = \frac{1}{as+b} \qquad \textit{i.e.} \qquad \hat{\omega}(s) = -\hat{h}(s)\hat{p}_{\rm L}(s) \tag{20}$$

with a and b being positive constants, if the corresponding storage frequency response function $\hat{c}(s)$ is given by (19) *with the following values of constants:*

$$A_1 = \tau_{\rm T}\,(a - 2H)\,, \tag{21a}$$
$$A_2 = b\tau_{\rm T} + a - 2H\,, \tag{21b}$$
$$A_3 = b - \alpha_{\rm g}\,. \tag{21c}$$

In this case, the system frequency will experience no Nadir and the steady-state frequency deviation $\Delta\omega$ and the RoCoF $|\dot{\omega}|_\infty$ will be determined by the following expressions:

$$\Delta\omega = -\frac{\Delta P}{b} \qquad \textit{and} \qquad |\dot{\omega}|_\infty = \frac{\Delta P}{a} \tag{22}$$

when $\hat{p}_{\rm L}(s) = \Delta P/s$.

Proof. Let the desired closed-loop transfer function from $-p_{\rm L}$ to ω be a first-order one given by (20). Then, using the explicit expression for the generator/turbine transfer function $\hat{g}(s)$ and (20), one can directly solve for the desired storage control strategy as

$$\frac{\hat{h}(s) - \hat{g}(s)}{\hat{h}(s)\hat{g}(s)} = -\frac{A_1 s^2 + A_2 s + A_3}{\tau_{\rm T} s + 1} =: \hat{c}_{\rm fs}(s) \tag{23}$$

with A_1, A_2, and A_3 given by (21).

Next, applying the initial and final value theorems to (20), we find that a and b satisfy the following relations:

$$|\dot{\omega}|_\infty = \Delta P \lim_{s\to\infty} s^2 \frac{\hat{h}(s)}{s} = \frac{\Delta P}{a}\,, \tag{24a}$$

$$\Delta\omega = -\,\Delta P \lim_{s\to 0} s\frac{\hat{h}(s)}{s} = -\frac{\Delta P}{b}\,, \tag{24b}$$

which are identical to (22). □

[5]As in VI control, an additional low-pass filter is also needed in frequency shaping control for the same reason.

Theorem 2 allows one to tune the storage frequency response strategy that guarantees Nadir-less response for the whole system while also providing the pre-set values for RoCoF and steady-state frequency deviation. However, such a tuning can lead to sub-optimal use of the storage capabilities if the system response without storage already provides satisfactory performance in terms of either RoCoF or steady-state frequency deviation (or both). Therefore, the actual tuning will depend on the existing system performance. Suppose the desired values of the RoCoF and steady-state frequency deviation are $|\dot{\omega}|_{\infty \rm d}$ and $\Delta\omega_{\rm d}$, respectively. Basically, if the response of the existing system suffices to provide satisfactory performance for RoCoF and/or steady-state frequency deviation, then one needs to adopt their actual values instead of the maximum allowed ones for tuning a and b. Overall, four cases are possible:

1) Case 1: System response suffices to provide satisfactory performance for both RoCoF and steady-state frequency deviation. In this case, one needs to use their actual values instead of the maximum allowed ones for tuning a and b. Thus, the optimal settings are:

$$a = 2H \qquad \text{and} \qquad b = \alpha_{\rm g}\,. \tag{25}$$

Here, the effect of storage is to eliminate frequency Nadir while keeping RoCoF and steady-state frequency deviation unchanged.

2) Case 2: System response suffices to provide satisfactory performance for RoCoF but not for steady-state frequency deviation – there is enough inertia but not enough primary response from generators. Then, a and b should be:

$$a = 2H \qquad \text{and} \qquad b = -\frac{\Delta P}{\Delta\omega_{\rm d}}. \tag{26}$$

3) Case 3: System response suffices to provide satisfactory steady-state frequency deviation but not RoCoF – there is enough primary response but not enough inertia. In this case:

$$a = \frac{\Delta P}{|\dot{\omega}|_{\infty \rm d}} \qquad \text{and} \qquad b = \alpha_{\rm g}.$$

4) Case 4: System response is insufficient to provide satisfactory steady-state frequency deviation and RoCoF – there is lack of both primary response and inertia. In this case:

$$a = \frac{\Delta P}{|\dot{\omega}|_{\infty \rm d}} \qquad \text{and} \qquad b = -\frac{\Delta P}{\Delta\omega_{\rm d}}.$$

All of the above discussed cases can be formulated compactly as:

$$a = \max\left(\frac{\Delta P}{|\dot{\omega}|_{\infty \rm d}}, 2H\right) \text{ and } b = \max\left(-\frac{\Delta P}{\Delta\omega_{\rm d}}, \alpha_{\rm g}\right), \tag{27}$$

with which the effect of the storage is to eliminate the frequency Nadir and at the same time improve the RoCoF and/or the steady-state frequency deviation if needed. For notational convenience, b can be parameterized with the surrogate variable $\alpha_{\rm b}$ defined in (16) as

$$b = \alpha_{\rm g} + \alpha_{\rm b}\,, \tag{28}$$

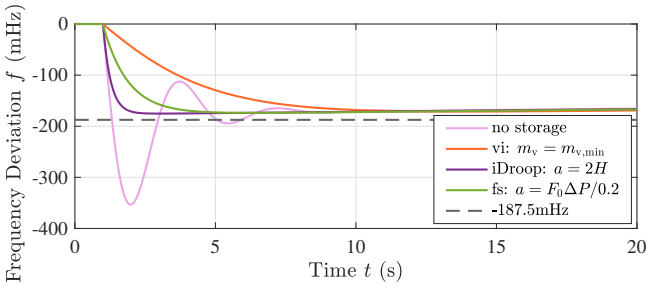

Fig. 6. Comparison of frequency deviations with Nadir eliminated under virtual inertia and frequency shaping control to a step power imbalance for $\alpha_b = 0$. Horizontal dashed line corresponds to the calculated steady-state value using generator inverse droop and power imbalance values.

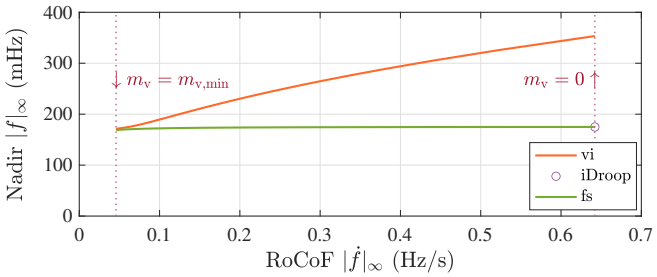

Fig. 7. Nadir as a function of RoCoF under frequency shaping control for $\alpha_b = 0$ and a within the range of $[2H, (2H + m_{v,min})]$.

which ensures a fair comparison between the frequency shaping control and the VI control by naturally setting the steady-state frequency deviation under the two controllers to be the same.

Note that, in the case that the existing system has enough inertia, i.e., $a = 2H$, the frequency shaping control reduces to the so-called iDroop with Nadir elimination tuning only – a dynamic droop control reported by us recently [23]:

$$\hat{c}_{\text{iDroop}}(s) = \frac{\alpha_g}{\tau_T s + 1} - (\alpha_g + \alpha_b) \ , \tag{29}$$

which eliminates the Nadir and improves the steady-state frequency deviation if needed, but does not affect the RoCoF.

The frequency shaping control, as its name suggests, makes the system frequency response effectively first-order, thus eliminating Nadir. Moreover, it also ensures that both RoCoF and steady-state frequency deviation are within the pre-specified limits $|\dot{\omega}|_{\infty d}$ and $\Delta\omega_d$, respectively. Fig. 6 illustrates the well-shaped frequency response under two different tunings of frequency shaping control compared with VI control (with $m_v = m_{v,min}$) and no storage base scenario. As for the two tunings of the frequency shaping control, the first one sets $a = 2H$ (corresponding to iDroop) so as to leave the RoCoF unchanged and the second one sets $a = F_0\Delta P/0.2$ in order to reduce the RoCoF to $0.2\,\text{Hz}\,\text{s}^{-1}$. For the Great Britain system, by setting $\alpha_g = 15\,\text{pu}$ in (28) for frequency shaping control, the frequency deviation is predicted by (22) to always stay above the value of steady-state frequency deviation given by $-187.5\,\text{mHz}$ following a power imbalance $\Delta P = 1.8\,\text{GW}$ ($0.056\,25\,\text{pu}$ on the system base), which matches the simulation results in Fig. 6.

To explicitly demonstrate the difference between frequency shaping control and VI, Fig. 7 shows Nadir as a function of the RoCoF. It is obvious that for VI those two metrics are coupled, while the frequency shaping control provides us the freedom to tune RoCoF without sacrificing Nadir elimination.

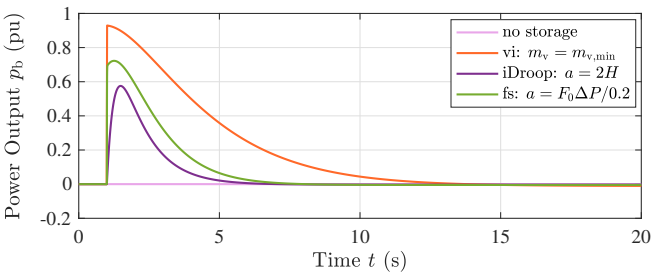

Fig. 8. Comparison of storage power transient responses with Nadir eliminated under virtual inertia, iDroop, and frequency shaping control to a step power imbalance for $\alpha_b = 0$. The corresponding frequency dynamics is shown in Fig. 6

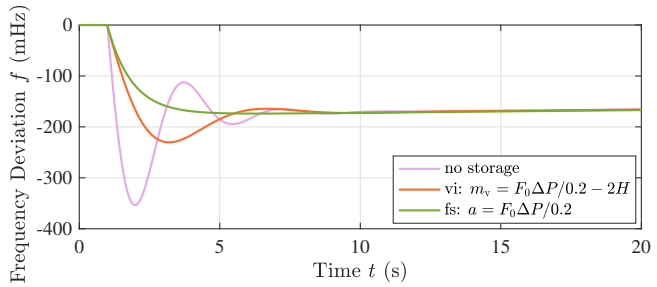

(a) Frequency deviations

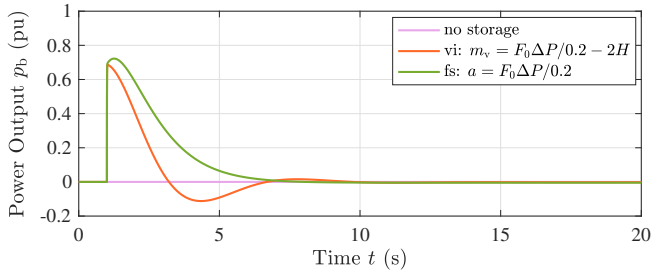

(b) Storage power transients

Fig. 9. Comparison of transient responses under virtual inertia and frequency shaping control to a step power imbalance for $\alpha_b = 0$ when the RoCoF is tuned to be $0.2\,\text{Hz}\,\text{s}^{-1}$.

B. Power and Energy Requirements on Storage

We next quantify the required amount of storage power to execute the frequency shaping control. Provided that the control is given by (19), the storage power output (following a step power imbalance) in Laplace domain is:

$$\hat{p}_{b,fs}(s) = -\frac{\Delta P}{s}\hat{h}(s)\hat{c}_{fs}(s) = \frac{\Delta P\left(A_1 s^2 + A_2 s + A_3\right)}{s\,(as+b)\,(\tau_T s + 1)} \ . \tag{30}$$

From here, an explicit (and rather cumbersome) expression for power in time domain can be found. Fig. 8 shows the storage power output as a function of time for the four control scenarios. Clearly, the proposed frequency shaping control outperforms the VI control – it requires up to 40% less storage power. In addition, the duration of the power peak is much shorter for frequency shaping control, which can allow to decrease the installed power of storage even more. Therefore, one crucial point is that the frequency shaping control makes better use of storage power than the VI control does. More precisely, unlike the VI control, under which a waste of considerable power on reducing the gentle enough RoCoF is a prerequisite for Nadir elimination, frequency shaping control finesses the issue without unnecessarily reducing the RoCoF.

To provide a more fair comparison, Fig. 9 plots the transient responses to a step power imbalance under the frequency shaping control (with $\alpha_{\rm b} = 0$) providing the RoCoF of $0.2\,{\rm Hz\,s^{-1}}$, and the VI control tuned to provide the same RoCoF value (without the purpose of Nadir elimination). In this case, the steady-state frequency deviation and the RoCoF are the same under the two controllers, thus, considering that the frequency shaping control significantly picks up the frequency drop, there is no surprise that it requires a somewhat higher peak power compared with the VI control. However, the frequency shaping control is clearly smarter since it trades slightly increased peak power for complete elimination of the frequency Nadir. Actually, the difference between the power curves of the two controllers can be understood as an approximation of the energy used by the frequency shaping control for Nadir elimination, whose amount is modest.

The energy capacity requirement for the frequency shaping control is mostly determined by the effective battery PFR constant $\alpha_{\rm b}$, similarly to VI control. For Cases 1 and 3 of the previous subsection, $\alpha_{\rm b} = 0$, and thus the energy requirement is very small and, like for VI, capacity will be mostly determined by the C-rate of batteries used.[6] In this regard, one might consider using different storage technologies (i.e., other than electro-chemical ESS) for realizing frequency shaping control. To name a few, two technologies, namely flywheels [25] and superconducting magnetic energy storage [26], [27], seem to be particularly suitable for this purpose. However, a more thorough economic analysis is required to assess their applicability and compare their use with that of electro-chemical ESS. For Cases 2 and 4, the storage is supposed to participate in the steady-state frequency response and the energy capacity requirement will be significantly higher. Similarly to VI control, it can be estimated as $E_{\rm b,max,fs} \approx \alpha_{\rm b}/K_{\rm I}$, where $\alpha_{\rm b} \equiv A_3 = b - \alpha_{\rm g}$ – the storage effective PFR constant.

The intuition behind the effectiveness of the frequency shaping control is that it is able to take the most advantage of the system natural frequency response capabilities. While VI can provide performance improvement for both RoCoF and Nadir, there is no way to decouple them in order to optimize the control effort. Frequency shaping control, on the contrary, provides IR only if it is needed to secure acceptable RoCoF value, and only with the minimum value needed. Frequency Nadir is then taken care of by a different contribution – iDroop, which is able to guarantee the effective first-order system dynamics. Therefore, frequency shaping control leverages the knowledge of the system inertia, primary response, and turbine dynamics in order to provide a more outstanding response by making full use of the system's own control capabilities.

[6]Energy requirements for frequency shaping control will be formally less than that for VI, but this is irrelevant in practice due to C-rate limitations.

C. Generalization to Multi-Machine Systems

Storage control strategy described by (19) was derived for a single-machine representation with a simplified model for generator turbine. Actually, the same methodology can be applied to deriving control strategy for more general cases. In this subsection we provide a generalization of the method for multi-machine systems with arbitrary models for governors and turbines.

We start from deriving the closed-loop power-frequency response for a multi-machine system. Let H_i be the inertia constant of the ith machine (for all the variables we denote machines by a lower index i) and $\hat{T}_i(s)$ be a combined transfer function of its governor and turbine, i.e., $\hat{p}_{{\rm m},i}(s) = -\alpha_{{\rm g},i}\hat{T}_i(s)\hat{\omega}_i(s)$. Note that $\hat{T}_i(0) = 1$ for every machine. Now, the multi-machine closed-loop frequency response to power imbalance is:

$$\hat{g}(s) = \frac{1}{\sum_i (2H_i s + \alpha_{{\rm g},i}\hat{T}_i(s))}\,. \tag{31}$$

Similarly to how we did before, we state that the additional storage frequency control strategy should transform the overall system response to an effective first-order form given by (20) with the constants a and b determining the system RoCoF and steady-state frequency deviation respectively. In the case of multi-machine system, the storage frequency response can be provided either in aggregated or fully decentralized way. In the latter case, one can think that each machine is "matched" by a corresponding storage response function $\hat{c}_i(s)$ of individual storage units in such a way that the overall system dynamics satisfies (20). Then, the following relation should be satisfied:

$$\sum_i (2H_i s + \alpha_{{\rm g},i}\hat{T}_i(s) - \hat{c}_i(s)) = as + b\,. \tag{32}$$

Let us now represent the response functions $\hat{c}_i(s)$ of individual storage units in the following way:

$$\hat{c}_i(s) = -(m_{{\rm v,i}}s - \alpha_{{\rm g},i}\hat{T}_i(s) + \alpha_{{\rm g},i} + \alpha_{{\rm b},i})\,, \tag{33}$$

where the first term represents the IR that is responsible for RoCoF and the other terms represent the dynamic droop that is responsible for Nadir and steady-state frequency deviation.

Derivation of the required values for $m_{\rm v,i}$ and $\alpha_{{\rm b},i}$ is somewhat similar to the derivation for a single-machine system. First of all, if the system's natural response is sufficient to provide satisfactory RoCoF and steady-state frequency response, then all $m_{\rm v,i}$ and $\alpha_{{\rm b},i}$ can be set to zero so that the control strategy for the storage units becomes:

$$\hat{c}_i(s) = \alpha_{{\rm g},i}\hat{T}_i(s) - \alpha_{{\rm g},i}\,. \tag{34}$$

In the case that either RoCoF or steady-state response (or both) needs to be improved by the storage, the required storage $m_{\rm v,i}$

and $\alpha_{\mathrm{b},i}$ can be determined from the following relations (we assume minimum required settings):

$$\sum_i m_{\mathrm{v,i}} = \frac{\Delta P}{|\dot{\omega}|_{\infty \mathrm{d}}} - 2\sum_i H_i, \tag{35a}$$

$$\sum_i \alpha_{\mathrm{b},i} = -\frac{\Delta P}{\Delta\omega_{\mathrm{d}}} - \sum_i \alpha_{\mathrm{g},i}\,. \tag{35b}$$

Here, $|\dot{\omega}|_{\infty \mathrm{d}}$ and $\Delta\omega_{\mathrm{d}}$ are the maximum allowed values of RoCoF and steady-state frequency deviation respectively (the latter will also correspond to frequency "Nadir" for first-order response). From the mathematical point of view, as long as (35) are satisfied, the assignment of individual values $m_{\mathrm{v,i}}$ and $\alpha_{\mathrm{b},i}$ can be done arbitrarily. From the practical point of view, contribution according to generator installed power might make sense. Another way, which could be more reasonable, is to set certain minimum requirements for generator inertia and droop gain, and then storage units are tuned to provide some additional $m_{\mathrm{v,i}}$ and/or $\alpha_{\mathrm{b},i}$ only for those generators that do not meet the threshold with their conventional capabilities.

Another important practical aspect is the tuning of storage units to provide the response $\hat{T}_i(s)$ that matches the corresponding governor-turbine dynamics. It is possible to tune the storage using the fully detailed governor model. However, even a simple second-order reduced model obtained from $\hat{T}_i(s)$ by balanced truncation procedure provides remarkably good performance, as we demonstrate in the validation section below.

V. Numerical Validation

In this section, we provide numerical validation for the performance of our developed frequency shaping control using more complex models for both of the energy storage and power system. First, we will use a more detailed representation of ESSs, explicitly modelling dynamics of interfacing converters with the phase-locked loop (PLL) and inner current control loop. Then, we will validate the performance of the frequency shaping control on a more realistic power system test case in Power System Toolbox (PST) [28] for Matlab.

A. Modelling of Voltage Source Converter

When developing the frequency shaping control strategy in the previous section, we have assumed that the measurements of the grid frequency are rather fast and accurate. Thus, we used the grid frequency as an input signal to our controller directly. Likewise, an assumption of rapid power injections by ESSs was made so that the ESSs are considered to follow our commands instantly. However, in reality, energy storage units are interfaced to the grid through power electronic converters, where voltage source converters (VSCs) are commonly applied. Therefore, we extend our modelling approach to explicitly account for VSC dynamics in this subsection.

Fig. 10 shows the configuration of a ESS feeding into the grid through a VSC with the frequency shaping control. Here, the main objective of the grid-following VSC acting as a current source is to adjust its power injection to the grid according to the grid frequency deviation at the bus where

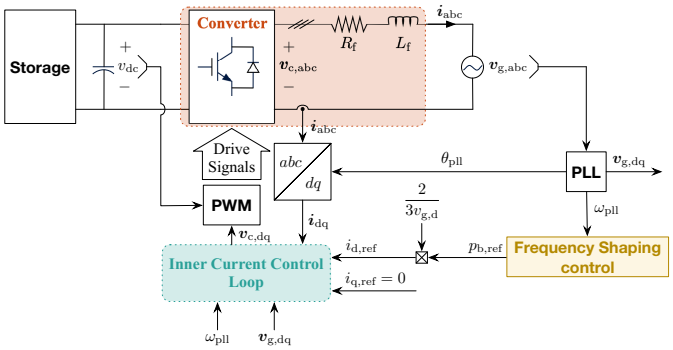

Fig. 10. ESS control scheme for realizing frequency shaping control.

it is located [14], [29]. With this aim, the VSC first measures the grid frequency deviation using a PLL, and then generates the current reference following the frequency shaping control, and finally yields the modulation reference that is fed to the pulse width modulation (PWM) from the inner current control loop.

We now discuss the elements mentioned above in more detail. We mostly follow the approach from [30], since the ESS models presented there are specifically derived and tested for power systems transient stability analysis. We also refer to [31]–[34].

B. Phase-Locked Loop and Power Controller

We adopt a typical synchronous reference frame PLL (SRF-PLL) [33] composed of a phase detector, a loop filter, and a voltage-controlled oscillator as shown in Fig. 11 to measure the grid frequency deviation.

- The phase detector provides the phase error information by transforming the three-phase grid voltages $\boldsymbol{v}_{\mathrm{g,abc}}$ from the abc natural reference frame to the dq synchronous reference frame. Here, we assume ideal grid conditions with neither unbalance nor harmonics, i.e,

$$\boldsymbol{v}_{\mathrm{g,abc}} := \begin{bmatrix} v_{\mathrm{g,a}} \\ v_{\mathrm{g,b}} \\ v_{\mathrm{g,c}} \end{bmatrix} = V_{\mathrm{g}} \begin{bmatrix} \cos(\theta_{\mathrm{g}}) \\ \cos\left(\theta_{\mathrm{g}} - \frac{2\pi}{3}\right) \\ \cos\left(\theta_{\mathrm{g}} + \frac{2\pi}{3}\right) \end{bmatrix}, \tag{36}$$

  where V_{g} and θ_{g} are the amplitude and phase of the grid voltages, respectively. Then the d- and q-axis components of the grid voltages are known to be

$$v_{\mathrm{g,d}} = V_{\mathrm{g}} \cos(\theta_{\mathrm{g}} - \theta_{\mathrm{pll}}), \tag{37a}$$

$$v_{\mathrm{g,q}} = V_{\mathrm{g}} \sin(\theta_{\mathrm{g}} - \theta_{\mathrm{pll}}), \tag{37b}$$

  where θ_{pll} is the estimated grid phase. Equation (37) indicates that the key to estimate θ_{g} is to keep $v_{\mathrm{g,q}}$ close to zero since $v_{\mathrm{g,q}} \approx V_{\mathrm{g}}(\theta_{\mathrm{g}} - \theta_{\mathrm{pll}}) \approx 0$ requires $\theta_{\mathrm{pll}} \approx \theta_{\mathrm{g}}$. It also follows that $v_{\mathrm{g,d}} \approx V_{\mathrm{g}}$, which means that $v_{\mathrm{g,d}}$ estimates the amplitude of the grid voltage. To make the PLL performance insensitive to variations in V_{g}, a normalization dividing $v_{\mathrm{g,q}}$ by v_{pll} is included [33], where v_{pll} is obtained by passing $v_{\mathrm{g,d}}$ through a low-pass filter with a cutoff frequency k_{v}, i.e.,

$$\hat{v}_{\mathrm{pll}} = \frac{k_{\mathrm{v}}}{s + k_{\mathrm{v}}} \hat{v}_{\mathrm{g,d}} \quad \text{or} \quad \dot{v}_{\mathrm{pll}} = k_{\mathrm{v}}(v_{\mathrm{g,d}} - v_{\mathrm{pll}}). \tag{38}$$

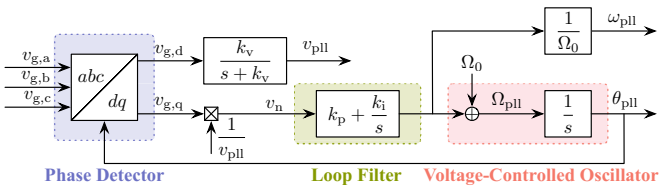

Fig. 11. Block diagram of the SRF-PLL.

- The loop filter forces $v_{\mathrm{g,q}}$ to zero through a proportional–integral controller. Thus, the estimated grid frequency deviation (in per unit) ω_{pll} is determined from the normalized $v_{\mathrm{g,q}}$, i.e., $v_{\mathrm{n}} := v_{\mathrm{g,q}}/v_{\mathrm{pll}}$, through the following dynamics

$$\Omega_0\hat{\omega}_{\mathrm{pll}} = \left(k_{\mathrm{p}} + \frac{k_{\mathrm{i}}}{s}\right)\hat{v}_{\mathrm{n}} \quad \text{or} \quad \Omega_0\dot{\hat{\omega}}_{\mathrm{pll}} = k_{\mathrm{p}}\dot{v}_{\mathrm{n}} + k_{\mathrm{i}}v_{\mathrm{n}}\,, \tag{39}$$

  where k_{p} and k_{i} are the proportional and integral gains.
- The voltage-controlled oscillator generates the estimated grid phase θ_{pll} via the integration of the estimated grid frequency (in radian per second) $\Omega_{\mathrm{pll}} := \Omega_0 + \Omega_0\omega_{\mathrm{pll}}$, i.e.,

$$\hat{\theta}_{\mathrm{pll}} = \frac{\hat{\Omega}_{\mathrm{pll}}}{s} \qquad \text{or} \qquad \dot{\theta}_{\mathrm{pll}} = \Omega_{\mathrm{pll}}\,. \tag{40}$$

Therefore, the PLL dynamics is included in our simulations through the model described by (37)–(40), where we set $k_{\mathrm{v}} = 140\,\mathrm{s}^{-1}$ [34], $k_{\mathrm{p}} = 8.4\,\mathrm{rad\,s}^{-1}$, and $k_{\mathrm{i}} = 100\,\mathrm{rad\,s}^{-2}$, corresponding to a bandwidth around $17.4\,\mathrm{rad\,s}^{-1}$ [32, Table 4.1].

The frequency shaping control plays the role of a real power controller. It maps the estimated grid frequency deviation ω_{pll} to a real power variation reference $p_{\mathrm{b,ref}}$ around the equilibrium operating point according to the law $\hat{c}_{\mathrm{fs}}(s)$ given in (19), where $p_{\mathrm{b,ref}}$ is used to generate the reference signals $i_{\mathrm{d,ref}}$ and $i_{\mathrm{q,ref}}$ for the current controller. Note that we assume that no reactive power control is executed by the converter (however, its inclusion in the scheme is rather straightforward). Thus, $i_{\mathrm{q,ref}} = 0$. Then, $i_{\mathrm{d,ref}}$ can be found from the real power expression $p_{\mathrm{b,ref}} = 3\left(v_{\mathrm{g,d}}i_{\mathrm{d,ref}} + v_{\mathrm{g,q}}i_{\mathrm{q,ref}}\right)/2$ as $i_{\mathrm{d,ref}} = 2p_{\mathrm{b,ref}}/\left(3v_{\mathrm{g,d}}\right)$.

C. Current Controller and Converter

We consider a conventional converter and inner current control loop in the dq-frame [30]–[32] with the block diagram as shown in Fig. 12. The dynamics of the d- and q-axis components of the converter output current $\boldsymbol{i}_{\mathbf{abc}}$ are given by

$$L_{\mathrm{f}}\dot{i}_{\mathrm{d}} = -R_{\mathrm{f}}i_{\mathrm{d}} + \omega_{\mathrm{pll}}L_{\mathrm{f}}i_{\mathrm{q}} + v_{\mathrm{c,d}} - v_{\mathrm{g,d}}\,, \tag{41a}$$
$$L_{\mathrm{f}}\dot{i}_{\mathrm{q}} = -R_{\mathrm{f}}i_{\mathrm{q}} - \omega_{\mathrm{pll}}L_{\mathrm{f}}i_{\mathrm{d}} + v_{\mathrm{c,q}} - v_{\mathrm{g,q}}\,, \tag{41b}$$

with R_{f} and L_{f} being the resistance and inductance of the converter output filter. Here, $\boldsymbol{v}_{\mathbf{c,dq}}$ are the converter output voltages before the filter in the dq-frame. A standard technique for decoupling i_{d} and i_{q} is to set [31]

$$\boldsymbol{v}_{\mathrm{c,dq}} := \begin{bmatrix} v_{\mathrm{c,d}} \\ v_{\mathrm{c,q}} \end{bmatrix} = \begin{bmatrix} u_{\mathrm{d}} - \omega_{\mathrm{pll}}L_{\mathrm{f}}i_{\mathrm{q}} + v_{\mathrm{g,d}} \\ u_{\mathrm{q}} + \omega_{\mathrm{pll}}L_{\mathrm{f}}i_{\mathrm{d}} + v_{\mathrm{g,q}} \end{bmatrix}, \tag{42}$$

where u_{d} and u_{q} are control signals to be chosen. Applying (42) to (41) yields

$$L_{\mathrm{f}}\dot{i}_{\mathrm{d}} = -R_{\mathrm{f}}i_{\mathrm{d}} + u_{\mathrm{d}} \qquad \text{and} \qquad L_{\mathrm{f}}\dot{i}_{\mathrm{q}} = -R_{\mathrm{f}}i_{\mathrm{q}} + u_{\mathrm{q}}\,,$$

where i_{d} and i_{q} are independent. Now, by choosing

$$\hat{u}_{\mathrm{d}} = \hat{K}_{\mathrm{c}}(s)\left(\hat{i}_{\mathrm{d,ref}} - \hat{i}_{\mathrm{d}}\right) = \frac{R_{\mathrm{f}} + sL_{\mathrm{f}}}{s\tau_{\mathrm{c}}}\left(\hat{i}_{\mathrm{d,ref}} - \hat{i}_{\mathrm{d}}\right)\,,$$
$$\hat{u}_{\mathrm{q}} = \hat{K}_{\mathrm{c}}(s)\left(\hat{i}_{\mathrm{q,ref}} - \hat{i}_{\mathrm{q}}\right) = \frac{R_{\mathrm{f}} + sL_{\mathrm{f}}}{s\tau_{\mathrm{c}}}\left(\hat{i}_{\mathrm{q,ref}} - \hat{i}_{\mathrm{q}}\right)\,,$$

we can compensate for the converter output filter dynamics so as to make

$$\hat{i}_{\mathrm{d}} = \frac{1}{\tau_{\mathrm{c}}s + 1}\hat{i}_{\mathrm{d,ref}} \qquad \text{and} \qquad \hat{i}_{\mathrm{q}} = \frac{1}{\tau_{\mathrm{c}}s + 1}\hat{i}_{\mathrm{q,ref}}$$

with the desired inner current control time constant τ_{c} typically around milliseconds. In our simulations, we set $\tau_{\mathrm{c}} = 1\,\mathrm{ms}$.

The power injection of the ESS to the grid under the frequency shaping control can be calculated by $p_{\mathrm{b,fs}} = 3\left(v_{\mathrm{g,d}}i_{\mathrm{d}} + v_{\mathrm{g,q}}i_{\mathrm{q}}\right)/2 \approx 3\left(v_{\mathrm{g,d}}i_{\mathrm{d}}\right)/2$, where $i_{\mathrm{q}} \approx 0$ is ensured by our setting that $i_{\mathrm{q,ref}} = 0$. Therefore, after considering the converter and inner current control loop, we can characterize the effective power response of the storage unit to the estimated grid frequency deviation as

$$\begin{aligned}\hat{p}_{\mathrm{b,fs}} \approx& \frac{3v_{\mathrm{g,d}}}{2}\hat{i}_{\mathrm{d}} = \frac{3v_{\mathrm{g,d}}}{2}\frac{1}{\tau_{\mathrm{c}}s + 1}\hat{i}_{\mathrm{d,ref}} \\ =& \frac{3v_{\mathrm{g,d}}}{2}\frac{1}{\tau_{\mathrm{c}}s + 1}\frac{2}{3v_{\mathrm{g,d}}}\hat{p}_{\mathrm{b,ref}} = \frac{\hat{c}_{\mathrm{fs}}(s)}{\tau_{\mathrm{c}}s + 1}\hat{\omega}_{\mathrm{pll}}.\end{aligned} \tag{43}$$

Last but not least, although in our simulations we use the nonlinear PLL model described by (37)–(40), we can substitute its linearized counterpart [33], [34], i.e.,

$$\hat{\omega}_{\mathrm{pll}} = \frac{k_{\mathrm{p}}s + k_{\mathrm{i}}}{s^2 + k_{\mathrm{p}}s + k_{\mathrm{i}}}\hat{\omega}\,,$$

to (43) to get a concise transfer function from the true grid frequency deviation to the power injection variation of the storage unit given by

$$\frac{\hat{p}_{\mathrm{b,fs}}}{\hat{\omega}} = \frac{k_{\mathrm{p}}s + k_{\mathrm{i}}}{s^2 + k_{\mathrm{p}}s + k_{\mathrm{i}}}\frac{\hat{c}_{\mathrm{fs}}(s)}{\tau_{\mathrm{c}}s + 1}. \tag{44}$$

For a device-level implementation, the control process abstracted by (44) is usually realized on a digital signal processor. The details of a device-level control realization are out of the scope of this paper.

D. Case Study

We test the performance of our frequency shaping control on the Western System Coordinating Council (WSCC) 9-bus 3-generator system given in Fig. 13, using the PST [28]. We use the system settings emulating the Great Britain system in the low-inertia scenario (see Table I), where the total system inertia is split slightly unevenly among three generators. As for the generators, although linear models are used in our analysis, sub-transient models with multi-stage turbines [35] equipped to realize the primary and secondary frequency control are adopted in our simulations, where the parameters of the turbines are chosen to be somewhat heterogenous to make the case more realistic.

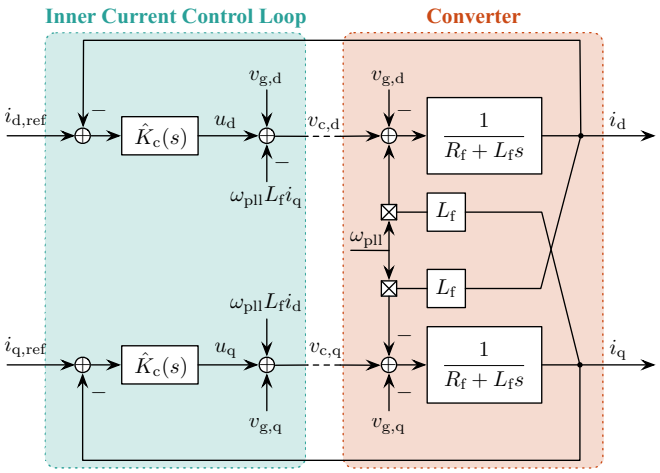

Fig. 12. Block diagam of the converter and inner current control loop in the dq-frame.

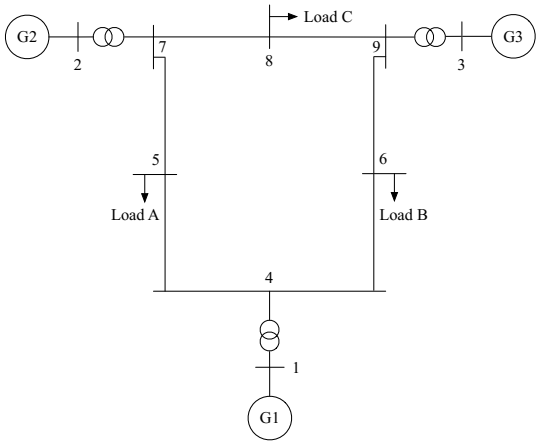

Fig. 13. 9-bus 3-generator WSCC test case used for validation of the frequency shaping control performance.

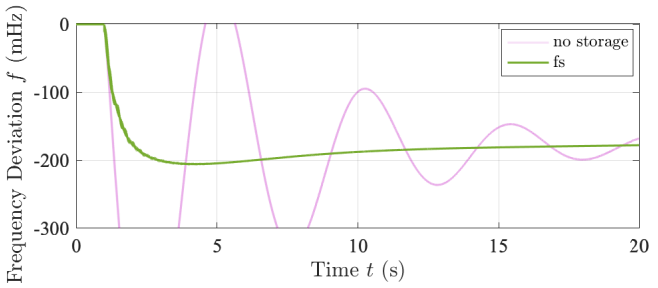

(a) Frequency deviations within 20 s

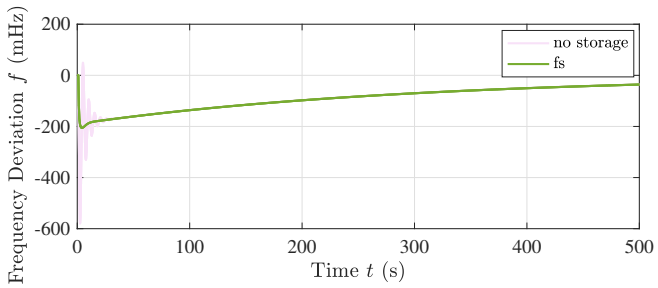

(b) Frequency deviations within 500 s

Fig. 14. Frequency shaping control compared to primary control only dynamics for storage units placed at buses 4, 7, and 9 for the WSCC test case.

The first scenario simulation is given by Fig. 14, where the three ESS units (with explicit converter models) are placed at buses 4, 7, and 9, respectively, with each unit tuned to match the response of the corresponding closest generator (i.e., generators 1, 2, and 3, respectively). For each ESS unit, the control settings are chosen in the form (33), with $\alpha_{\mathrm{b},i} = 0$ and $\hat{T}_i(s)$ chosen to match the dynamics of the nearest generator turbine using the second-order reduced turbine model obtained via balanced truncation. Additional IR $m_{\mathrm{v,i}}$ is only deployed at bus 7 since only the corresponding generator 2 is assumed to have insufficient inertia constant. Note that the ESS units are placed not at the generator buses but at the neighbouring ones, taking as inputs to their PLLs the local bus voltage not the actual machine frequencies.

Observe from Fig. 14 that the frequency shaping control provides the frequency responses that are very close to the desired first-order ones with the constraints on the RoCoFs and steady-state frequency deviations satisfied. A minimal Nadir of about 20 mHz below the quasi-steady-state frequency deviation can be seen, which is most likely due to the fact that generator and governor/turbine parameters are heterogenous or that reduced turbine models are used for control design. Yet, we highlight that this small residual Nadir can be effectively removed by re-tuning the frequency shaping control to somewhat conservative turbine time constants as discussed later. Note that the swings of individual generators are visible only upon closer inspection since the amplitudes of their oscillations in respect to the system COI trajectory are rather small – they all follow the COI trajectory well.

To investigate the impact of the placement of ESS units on the system performance under frequency shaping control, we modified the first scenario by placing all three ESS units at bus 7, while keeping their control settings unchanged. Fig. 15 shows the frequency deviations in this scenario, which exhibit a minimal difference from those in the first scenario. This implies that the system performance is not very sensitive to the placement of ESS units. However, we emphasize that there could be additional constraints associated with the local grid strength on the placement of ESS units. More precisely, since the frequency shaping control assumes a rather high power response during contingencies, one has to guarantee that the grid is sufficiently strong at the placement site in order to avoid possible stability issues [36] resulting from PLLs.

Next, we proceed to examine the robustness performance of the frequency shaping control under limited knowledge of the governor/turbine parameters. Fig. 16 shows the frequency dynamics of a WSCC system with the same placement of ESS units as in Fig. 14, where we assume that the frequency shaping control is designed based on estimated values of turbine time constants that are not necessarily exactly equal to the true values. Three cases are considered here – the estimated values are equal to (green line), smaller than (blue line), or greater than (gray line) the true values. The last case is deemed

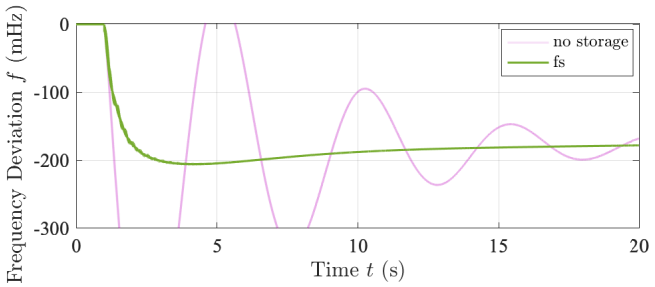

(a) Frequency deviations within 20 s

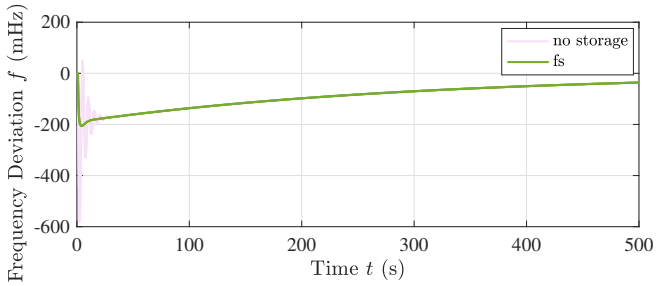

(b) Frequency deviations within 500 s

Fig. 15. Same as Fig. 14, but all the ESS units are placed at bus 7 (keeping their original control settings).

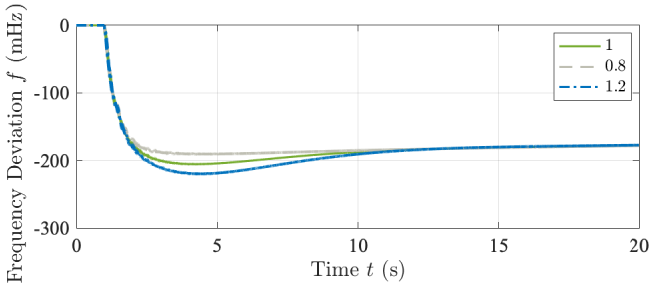

Fig. 16. Frequency deviations under frequency shaping control designed using different estimated values of turbine time constants, where the legends denote the ratios of true to estimated turbine time constants.

to be conservative since a Nadir-less control is possible to be achieved, from which a rule of thumb for frequency shaping control design can be obtained. That is, in the design, we should assume that the response time of turbines is longer than what it really is, otherwise the Nadir is more pronounced.

Finally, in order to illustrate the performance of the frequency shaping control in the case of multiple areas, we modify the existing WSCC test case (see Fig. 13) by increasing the impedance of the lines $4-6$ and $5-7$ to 10 times its value, which results in a distinct 2-area system. Fig. 17 and Fig. 18 show the frequency dynamics of this artificial 2-area system in the two scenarios of the placement of ESS units same as those in Fig. 14 and Fig. 15, respectively. Clearly, swings among generators are quite pronounced in both scenarios, compared to those in the original compact system. Moreover, in this case, the actual placement of ESS units affects the amplitudes of swings during the frequency transients. Specifically, swings become larger under the "uneven" ESS placement. Nevertheless, the overall control performance remains very good even under this scenario.

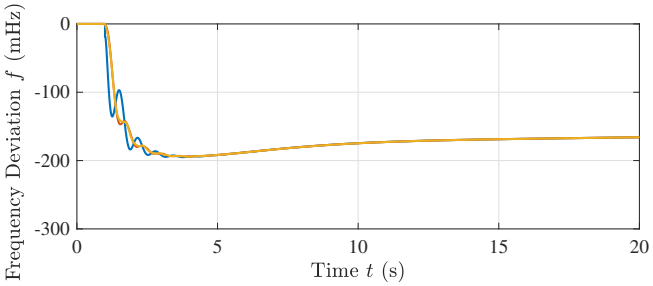

Fig. 17. Frequency deviations under shaping control for an impedance-increased WSCC test case with ESS units placed at buses 4, 7, and 9.

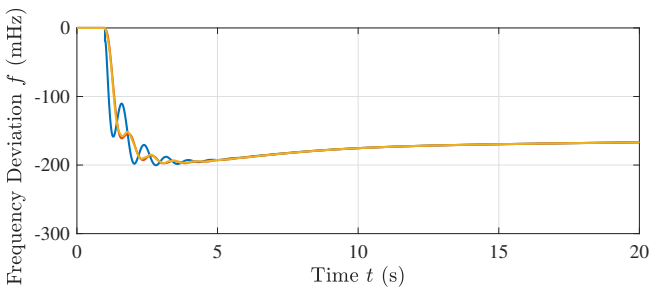

Fig. 18. Frequency deviations under shaping control for an impedance-increased WSCC test case with all ESS units placed at bus 7.

VI. Conclusions

We have presented a new type of frequency control strategy for energy storage units, which allows to completely eliminate frequency Nadir by making the system dynamics effectively first-order. Our control method significantly outperforms the conventional VI control, requiring less storage power output (40% less on one of the test cases), while also significantly reducing the duration of the peak-power response. The effectiveness of our strategy is based on its ability to utilize the system frequency response capability, effectively withdrawing the storage response as the generator turbine increases its power output. Such a Nadir-less dynamics can allow to completely revise the security assessment procedures, which can now be done using simple *algebraic* calculations, rather than dynamic simulations. Such an approach can be especially valuable for microgrids, where performing dynamic simulations on a regular basis can be problematic. Moreover, we envision that the "shaping" of power-frequency response of generators by storage units can provide benefits beyond the frequency control itself. Some straightforward applications include mitigation of turbine effort for frequency control as well as small-signal and transient stability enhancements.

The proposed control strategy was tested on a realistic system setup, with more complex generator and governor/turbine models as well as explicit modelling of the ESS converter dynamics. It appeared that most of the properties of the control strategy are preserved even when these complex models are used. Although the frequency responses are not strictly first-order, the deviations of the frequency dynamics of individual generators from the ideal first-order response are rather small. We note, though, that the placement of ESS units appeared to have certain influence on the control performance for multiple-

area systems, with the best performance being achieved when each ESS unit is placed near the generator whose turbine dynamics it is tuned to match. Thus, an idea of a *generator-storage* complex units becomes attractive – such complex units can have a much better power-frequency response that provides the overall almost first-order system frequency dynamic performance.

Although the frequency shaping control development was inspired by low-inertia large-scale power systems, it has the potential to be applied to microgrids. Particularly, the absence of long connection lines makes microgrids ideal for realization of frequency shaping control, which offers good potential for significantly reducing the reserve capacity requirements so as to drive the costs for microgrid deployment down. We note, though, that additional research might be needed for super low-inertia microgrids or even zero-inertia systems that are fully converter-based, where the interaction among multiple converters can become significant, imposing certain limits on control settings.

REFERENCES

[1] F. Milano, F. Dörfler, G. Hug, D. J. Hill, and G. Verbič, "Foundations and challenges of low-inertia systems (invited paper)," in *Proc. of Power Systems Computation Conference*, June 2018, pp. 1–25.

[2] S. Püschel-L, P. Mancarella *et al.*, "Mapping the frequency response adequacy of the Australian national electricity market," in *Proc. of Australasian Universities Power Engineering Conference*, Nov. 2017, pp. 1–6.

[3] "All island TSO facilitation of renewables studies," EirGrid, Tech. Rep., 2010.

[4] J. O'Sullivan, A. Rogers, D. Flynn, P. Smith, A. Mullane, and M. O'Malley, "Studying the maximum instantaneous non-synchronous generation in an island system–frequency stability challenges in Ireland," *IEEE Transactions on Power Systems*, vol. 29, no. 6, pp. 2943–2951, Nov. 2014.

[5] F. Sánchez, F. Gonzalez-Longatt, and J. L. Rueda, "Security assessment of system frequency response," in *Proc. of IEEE Power & Energy Society General Meeting*, Aug. 2019, pp. 1–5.

[6] D. Greenwood, K. Y. Lim, C. Patsios, P. Lyons, Y. S. Lim, and P. Taylor, "Frequency response services designed for energy storage," *Applied Energy*, vol. 203, pp. 115–127, Oct. 2017.

[7] "Technical report on the events of 9 August 2019," National Grid ESO, Tech. Rep., 2019.

[8] J. Fang, H. Li, Y. Tang, and F. Blaabjerg, "Distributed power system virtual inertia implemented by grid-connected power converters," *IEEE Transactions on Power Electronics*, vol. 33, no. 10, pp. 8488–8499, Oct. 2018.

[9] P. Tielens and D. Van Hertem, "The relevance of inertia in power systems," *Renewable and Sustainable Energy Reviews*, vol. 55, pp. 999–1009, Mar. 2016.

[10] U. Tamrakar, D. Shrestha, M. Maharjan, B. P. Bhattarai, T. M. Hansen, and R. Tonkoski, "Virtual inertia: Current trends and future directions," *Applied Sciences*, vol. 7, no. 7, 2017.

[11] M. F. M. Arani and E. F. El-Saadany, "Implementing virtual inertia in DFIG-based wind power generation," *IEEE Transactions on Power Systems*, vol. 28, no. 2, pp. 1373–1384, May 2013.

[12] P. R. Almeida, F. J. Soares, and J. P. Lopes, "Electric vehicles contribution for frequency control with inertial emulation," *Electric Power Systems Research*, vol. 127, pp. 141–150, Oct. 2015.

[13] S. S. Guggilam, C. Zhao, E. Dall'Anese, Y. C. Chen, and S. V. Dhople, "Optimizing DER participation in inertial and primary-frequency response," *IEEE Transactions on Power Systems*, vol. 33, no. 5, pp. 5194–5205, Sept. 2018.

[14] B. K. Poolla, D. Groß, and F. Dörfler, "Placement and implementation of grid-forming and grid-following virtual inertia and fast frequency response," *IEEE Transactions on Power Systems*, vol. 34, no. 4, pp. 3035–3046, July 2019.

[15] J. O'Sullivan, M. Power, M. Flynn, and M. O'Malley, "Modelling of frequency control in an island system," in *Proc. of Power Engineering Society 1999 Winter Meeting*, vol. 1, Jan. 1999, pp. 574–579.

[16] G. Lalor, J. Ritchie, D. Flynn, and M. J. O'Malley, "The impact of combined-cycle gas turbine short-term dynamics on frequency control," *IEEE Transactions on Power Systems*, vol. 20, no. 3, pp. 1456–1464, Aug. 2005.

[17] A. Ulbig, T. S. Borsche, and G. Andersson, "Impact of low rotational inertia on power system stability and operation," *IFAC Proceedings Volumes*, vol. 47, no. 3, pp. 7290–7297, 2014.

[18] "System operability framework 2016," National Grid Electricity System Operator, Tech. Rep., Nov. 2016. [Online]. Available: https://www.nationalgrideso.com/document/63476/download

[19] "National electricity transmission system security and quality of supply standard," National Grid Electricity System Operator, Tech. Rep., Apr. 2019. [Online]. Available: https://www.nationalgrideso.com/document/141056/download

[20] V. Knap, S. K. Chaudhary, D.-I. Stroe, M. Swierczynski, B.-I. Craciun, and R. Teodorescu, "Sizing of an energy storage system for grid inertial response and primary frequency reserve," *IEEE Transactions on Power Systems*, vol. 31, no. 5, pp. 3447–3456, Sept. 2015.

[21] W. Wei, Z. Wang, F. Liu, M. Shafie-khah, and J. P. S. Catalão, "Cost-efficient deployment of storage unit in residential energy systems," *IEEE Transactions on Power Systems*, vol. 36, no. 1, pp. 525–528, Jan. 2021.

[22] "Continental europe operation handbook: P1—policy 1: Load-frequency control and performance [C]," Union for the Coordination of Transmission of Electricity, Tech. Rep., 2009.

[23] Y. Jiang, R. Pates, and E. Mallada, "Dynamic droop control in low-inertia power systems," *IEEE Transactions on Automatic Control*, (Accepted).

[24] "A guide to understanding battery specifications," *MIT Electric Vehicle Team*, 2008.

[25] M. L. Lazarewicz and A. Rojas, "Grid frequency regulation by recycling electrical energy in flywheels," in *Proc. of IEEE Power Engineering Society General Meeting*, June 2004, pp. 1–5.

[26] V. S. Vulusala G and S. Madichetty, "Application of superconducting magnetic energy storage in electrical power and energy systems: a review," *International Journal of Energy Research*, vol. 42, no. 2, pp. 358–368, Feb. 2018.

[27] P. Breeze, *Power system energy storage technologies*. Academic Press, 2018.

[28] J. H. Chow and K. W. Cheung, "A toolbox for power system dynamics and control engineering education and research," *IEEE transactions on Power Systems*, vol. 7, no. 4, pp. 1559–1564, Nov. 1992.

[29] J. Rocabert, A. Luna, F. Blaabjerg, and P. Rodríguez, "Control of power converters in ac microgrids," *IEEE Transactions on Power Electronics*, vol. 27, no. 11, pp. 4734–4749, Nov. 2012.

[30] A. Ortega and F. Milano, "Generalized model of VSC-based energy storage systems for transient stability analysis," *IEEE transactions on Power Systems*, vol. 31, no. 5, pp. 3369–3380, Sept. 2016.

[31] A. Yazdani and R. Iravani, *Voltage-sourced converters in power systems: modeling, control, and applications*. John Wiley & Sons, 2010.

[32] Y. Sun, "The impact of voltage-source-converters' control on the power system: the stability analysis of a power electronics dominant grid," Ph.D. dissertation, 2018.

[33] S. Golestan, J. M. Guerrero, and J. C. Vasquez, "Three-phase PLLs: A review of recent advances," *IEEE Transactions on Power Electronics*, vol. 32, no. 3, pp. 1894–1907, Mar. 2017.

[34] S. Golestan and J. M. Guerrero, "Conventional synchronous reference frame phase-locked loop is an adaptive complex filter," *IEEE Transactions on Industrial Electronics*, vol. 62, no. 3, pp. 1679–1682, Mar. 2015.

[35] H. Chávez, R. Baldick, and S. Sharma, "Governor rate-constrained OPF for primary frequency control adequacy," *IEEE Transactions on Power Systems*, vol. 29, no. 3, pp. 1473–1480, May 2014.

[36] D. Dong, B. Wen, D. Boroyevich, P. Mattavelli, and Y. Xue, "Analysis of phase-locked loop low-frequency stability in three-phase grid-connected power converters considering impedance interactions," *IEEE Transactions on Industrial Electronics*, vol. 62, no. 1, pp. 310–321, Jan. 2015.

Yan Jiang is currently working toward the Ph.D. degree at the Department of Electrical and Computer Engineering and the M.S.E. degree at the Department of Applied Mathematics and Statistics, Johns Hopkins University. She received the B.Eng. degree in electrical engineering and automation from Harbin Institute of Technology in 2013, and the M.S. degree in electrical engineering from Huazhong University of Science and Technology in 2016. Her research interests lie in the area of control of power systems.

Eliza Cohn earned her Bachelors of Science degree (with honors) in Electrical Engineering and Mathematics from Johns Hopkins University in 2020. She is the recipient of the Muly Family Undergraduate Research Award from the Department of Electrical and Computer Engineering in 2019, the Provost's Undergraduate Research Award in 2018, and the Huggins ECE Fellowship also in 2018. Currently, she is working as a data scientist and software engineer for a healthcare company based in Raleigh, NC. Her research interests include control systems analysis and design, power systems, digital signal processing, and reinforcement learning.

Petr Vorobev (M'15) received his Ph.D. degree in theoretical physics from Landau Institute for Theoretical Physics, Moscow, in 2010. Currently, he is an Assistant Professor at Skolkovo Institute of Science and Technology (Skoltech), Moscow, Russia. Before joining Skoltech, he was a Postdoctoral Associate at the Mechanical Engineering Department of Massachusetts Institute of Technology (MIT), Cambridge, MA. His research interests include a broad range of topics related to power system dynamics and control. This covers low frequency oscillations in power systems, dynamics of power system components, multi-timescale approaches to power system modelling, development of plug-and-play control architectures for microgrids.

Enrique Mallada (S'09-M'13-SM') is an Assistant Professor of Electrical and Computer Engineering at Johns Hopkins University. Prior to joining Hopkins in 2016, he was a Post-Doctoral Fellow in the Center for the Mathematics of Information at Caltech from 2014 to 2016. He received his Ingeniero en Telecomunicaciones degree from Universidad ORT, Uruguay, in 2005 and his Ph.D. degree in Electrical and Computer Engineering with a minor in Applied Mathematics from Cornell University in 2014. Dr. Mallada was awarded the Catalyst Award in 2020 and the Discovery Award in 2019 from Johns Hopkins University, the NSF CAREER award in 2018, the ECE Director's PhD Thesis Research Award for his dissertation in 2014, the Center for the Mathematics of Information (CMI) Fellowship from Caltech in 2014, and the Cornell University Jacobs Fellowship in 2011. His research interests lie in the areas of control, dynamical systems and optimization, with applications to engineering networks such as power systems and the Internet.